International Journal of Electronics and Communication Engineering (IJECEG)
Volume 2, Issue 1, January-June 2025, pp. 24-47, Article ID: IJECEG_02_01_003
Available online at https://iaeme.com/Home/issue/IJECEG?Volume=2&Issue=1
Journal ID: 1556-1522; DOI: https://doi.org/10.34218/IJECEG_02_01_003

RESOLUTION, COMPUTATIONAL EFFICIENCY, AND COST ANALYSIS OF BACKPROPAGATION AND HOLOGRAPHIC ALGORITHMS FOR CONCEALED OBJECT DETECTION THROUGH VARIOUS MATERIALS USING MONOSTATIC MICROWAVE IMAGING

Babatunde Olatujoye[1*], Binbin Yang[2]
[1,2]Department of Electrical and Computer Engineering, North Carolina A&T State University, Greensboro, USA.
***Corresponding Author: Babatunde Olatujoye**

ABSTRACT

Microwave imaging is a non-invasive and non-ionizing technique with significant applications in security screening, material characterization, and non-destructive testing. This study presents a monostatic microwave imaging system utilizing an ultra-wideband (UWB) horn antenna operating between 15 GHz and 22 GHz to detect concealed metallic targets behind various materials. The experimental setup employed a Vector Network Analyzer (VNA) to measure the backscattered S-parameters while an automated two-dimensional (2-D) scanner systematically moved the antenna across a 50 cm × 50 cm aperture with a 1 cm step size. Different concealment materials, including dry cloth, wet cloth, wood, granite, and tiles of varying thicknesses, were introduced to evaluate their effects on target visibility and image quality. Two image

reconstruction techniques—Backpropagation Algorithm (BPA) and Holographic (FFT-based) processing—were applied to the measured data to assess their performance in terms of spatial resolution, computational efficiency, and noise suppression. The BPA demonstrated superior spatial resolution, effectively resolving the shapes and locations of the targets, while the FFT-based method provided faster image reconstruction, making it more suitable for large-scale imaging. These findings contribute to the development of high-resolution and computationally efficient microwave imaging techniques for concealed object detection in security and industrial applications.

Keywords: Backpropagation Algorithm (BPA), Concealed Object Detection, Cross Range Plot, Holographic Imaging, Ultra-Wideband (UWB), Microwave Imaging, Monostatic, Signal-to-Clutter Ratio (SCR).

Cite this Article: Babatunde Olatujoye, Binbin Yang. (2025). Resolution, Computational Efficiency, and Cost Analysis of Backpropagation and Holographic Algorithms for Concealed Object Detection Through Various Materials Using Monostatic Microwave Imaging. *International Journal of Electronics and Communication Engineering (IJECEG)*, 2(1), 24-47.

https://iaeme.com/MasterAdmin/Journal_uploads/IJECEG/VOLUME_2_ISSUE_1/IJECEG_02_01_003.pdf

1. Introduction

The need for efficient and high-resolution imaging techniques for concealed object detection (COD) has become increasingly critical in various security and industrial applications. Microwave imaging (MWI) has emerged as a promising non-destructive technique for detecting objects hidden behind different materials, using its ability to penetrate dielectric barriers while maintaining a reasonable spatial resolution [1]. Among MWI techniques, monostatic microwave imaging stands out due to its compact system design, reduced hardware complexity, and cost-effectiveness compared to bistatic or multistatic configurations [2]. However, the effectiveness of monostatic MWI for COD depends heavily on the imaging algorithm employed, which must balance resolution, computational efficiency, and cost.

Two prominent algorithmic approaches for monostatic microwave imaging are backpropagation (BP) and holographic imaging techniques. The backpropagation algorithm is widely used due to its simplicity and ability to reconstruct images with relatively high

resolution by iteratively refining estimates of the object's position based on received microwave signals [3]. However, despite its advantages, BP algorithms often suffer from high computational complexity, making real-time applications challenging [4]. On the other hand, holographic imaging techniques exploit phase information to generate high-fidelity images with reduced computational demands. Still, they may introduce limitations in in-depth resolution and sensitivity when dealing with varying material properties [5]. The choice between these algorithms thus requires a trade-off analysis between resolution, computational efficiency, and cost.

A significant challenge in COD applications is the influence of different barrier materials on microwave signal propagation and attenuation. Materials such as wood, plastic, concrete, and composite structures exhibit distinct electromagnetic properties that affect wave transmission, reflection, and scattering [6]. Consequently, the performance of BP and holographic algorithms may vary depending on the material through which the concealed object is detected. Consequently, an in-depth analysis of how these algorithms perform under different material conditions is essential for optimizing their practical deployment in security screening, industrial inspection, and biomedical imaging applications [7].

This study aims to conduct a comparative evaluation of backpropagation and holographic algorithms for concealed object detection using monostatic microwave imaging. Specifically, the research focuses on analyzing their resolution capabilities, computational efficiency, and associated costs when applied to various material environments. In quantifying these performance metrics, this study provides valuable insights into selecting the most suitable algorithm for different real-world applications.

The remaining sections of this paper are structured as follows: Section 2 presents a review of related works, discussing existing research on microwave imaging, backpropagation, and holographic algorithms. Section 3 details the materials and methods used in this study, including system configuration and algorithm implementation. Section 4 presents and discusses the obtained results, highlighting key performance trade-offs. Finally, Section 5 concludes the study with a summary of findings and recommendations for future research.

2. Review of Related Works

The growing demand for COD through diverse materials has spurred extensive research into MWI techniques. Chen *et al*. [1] explored MWI's penetration capabilities using frequency-

domain simulations and experimental measurements across wood, plastic, and concrete barriers. Their findings established that MWI could detect objects behind materials up to 30 cm thick, though resolution degraded significantly at greater depths. However, their study lacked an analysis of computational efficiency, focusing instead on validating penetration potential. Complementing this, [2] compared monostatic, bistatic, and multistatic MWI configurations, highlighting that monostatic systems reduced hardware costs by 40% but achieved 15% lower resolution than multistatic setups. Their work emphasized cost-resolution trade-offs but did not propose algorithmic adjustments to mitigate resolution losses in monostatic systems.

Gurbuz *et al*. [3] advanced BP algorithms by implementing a time-domain iterative approach for COD, achieving sub-wavelength resolution ($\sim\lambda/5$). However, their method required three times more computation time than conventional techniques, rendering it impractical for real-time applications.

Addressing computational bottlenecks, Zhang and Zhao [4] introduced GPU-accelerated BP, reducing processing time by 60%. Despite this improvement, their approach suffered a 20% resolution drop when imaging objects behind metal-rich barriers, emphasizing unresolved trade-offs between speed and accuracy in heterogeneous environments.

In contrast, Kim *et al*. [5] developed a holographic MWI technique using phase retrieval and Fourier transforms, enabling real-time processing ($0.2\ sec/image$). However, their method exhibited depth localization errors exceeding 10% in multi-layered materials, revealing limitations in handling material complexity.

Material properties significantly influence MWI performance, as shown by [6], who measured microwave attenuation across 15 materials. They reported up to $50\ dB/m$ attenuation in conductive barriers like reinforced concrete, severely degrading signal-to-noise ratios. Their study, however, did not integrate these findings into adaptive imaging algorithms.

Expanding on practical applications, [7] conducted a cost-benefit analysis of BP and holography, identifying holography as cost-effective for airport security but favouring BP in medical imaging due to superior resolution. Their review highlighted the absence of cross-material comparative studies to guide algorithm selection in hybrid environments.

Wang *et al*. [8] attempted to merge BP and holography in a hybrid approach, using BP for coarse imaging and holography for refinement. While this improved depth resolution by 25%, the reliance on FPGA-based hardware escalated costs, limiting scalability for budget-constrained applications.

Recent innovations include [9], who applied compressive sensing to holographic MWI, reducing data acquisition by 70% through sparse recovery. Their method halved acquisition time but failed to reconstruct objects behind multi-layered barriers (like plastic-concrete composites), indicating a need for adaptive sparsity models.

Patel *et al*. [10] introduced a machine learning-enhanced BP algorithm, training a convolutional neural network (CNN) to refine BP outputs. Their hybrid model reduced computational time by 45% while maintaining resolution, though training data were limited to homogeneous materials like drywall.

O'Connor *et al*. [11] analyzed MWI for multi-layered barriers, proposing a frequency-hopping technique to mitigate attenuation. Their simulations showed a 30% improvement in depth resolution but required specialized wideband antennas, increasing system costs.

Lastly, [12] evaluated adaptive holography for dynamic environments, dynamically adjusting phase correction based on material permittivity. Their experiments reduced depth errors to 5% in heterogeneous materials but demanded continuous calibration, complicating real-world deployment.

Collectively, these studies highlight critical gaps: (1) insufficient optimization of BP and holography for multi-material or composite barriers, (2) unresolved trade-offs between computational efficiency and resolution in real-time systems, and (3) limited cost-benefit analyses of algorithm-hardware synergies.

2.1 Back Propagation Image Reconstruction Algorithm

This time-domain method back-propagates received signals to the target plane using Green's functions. It assumes homogeneous media, limiting accuracy in heterogeneous environments [13]. Grzegorczyk *et al*. [14] improved robustness by incorporating iterative Born approximations, achieving 90% fidelity in wall-penetrating imaging.

Theory of Signal Model

According to [15], the development of a suitable signal model is crucial in the use of any imaging algorithm. In this study, the frequency is discretized by steps Δf. In complex representation, the transmitted signal can be expressed as given in (1).

$$s_{Tx}(t) = \sum_{n=0}^{N_f-1} e^{-j2\pi(f_0+n\Delta f)t}\,\mathrm{rect}\left(\frac{t}{T}-n\right) \quad (1)$$

where T is the dwell time of each of the N_f discreet frequency steps. Assuming a point target at location r , the delay of the received signal is expressed in (2).

$$\tau(r) = \frac{1}{c_0}(|r - r_{Tx}| + |r - r_{Rx}|) \quad (2)$$

This depends solely on the respective antenna positions, τ. The delayed received reflected signal is mixed with the transmitted signal, and the frequency domain output signal is expressed in (3).

$$S(r_{Tx}, r_{Rx}, f_n) = \Gamma e^{-j2\pi f_n \tau(r)} \quad (3)$$

This signal only depends on the delay, τ and the reflectivity of the target Γ. However, for a distributed target with reflectivity $o\ (r)$, the received signal is given in (4).

The basic idea of the MI system is circles measuring the electromagnetic energy reflected from a target. In a monostatic configuration, a single antenna serves as both the transmitter and receiver, moving across a 2D aperture defined by *X* and *Y* coordinates. The target object absorbs a portion of the energy while the remaining part is reflected to the antenna, which captures this reflected signal to calculate inverse-scattering parameters for image creation.

This study explored an imaging technique based on the backpropagation algorithm, wherein the antenna is positioned over the *X* and *Y* axes, allowing electromagnetic energy to propagate along the Z axis. When a target is located along the Z axis at a distance *z* from the antenna, the scattering function $S(r)$ describes the points reflecting energy to the antenna. The data received (amplitude and phase) includes electric field values as a function of the microwave signals' travel time. The total flight time is the round-trip time from the transmitting antenna to a point on the target and back, as illustrated in Fig. 1. The phase history data for a single-point target is given in (4) [16], [17].

$$o(\bar{r}) = \sum_{N_\omega} \sum_{N_A} s(\vec{r}_A, \omega) e^{j2\frac{\omega}{c_0}R} \quad (4)$$

where $s(\bar{r}_A, \omega)$ denotes the received complex signal at location $\bar{r}_A$ and angular frequency ω, and $o(\bar{r})$ is the desired reflectivity distribution of the device under test, DUT, which is the target. $R = |\bar{r}_A - \vec{r}|$ is the distance between position $\bar{r}_A$ of the respective antenna

element and the position of $\vec{r}$ of the points on the target. A practical imaging system possesses a limited number of transmit-receive (TR) combinations (pairs).

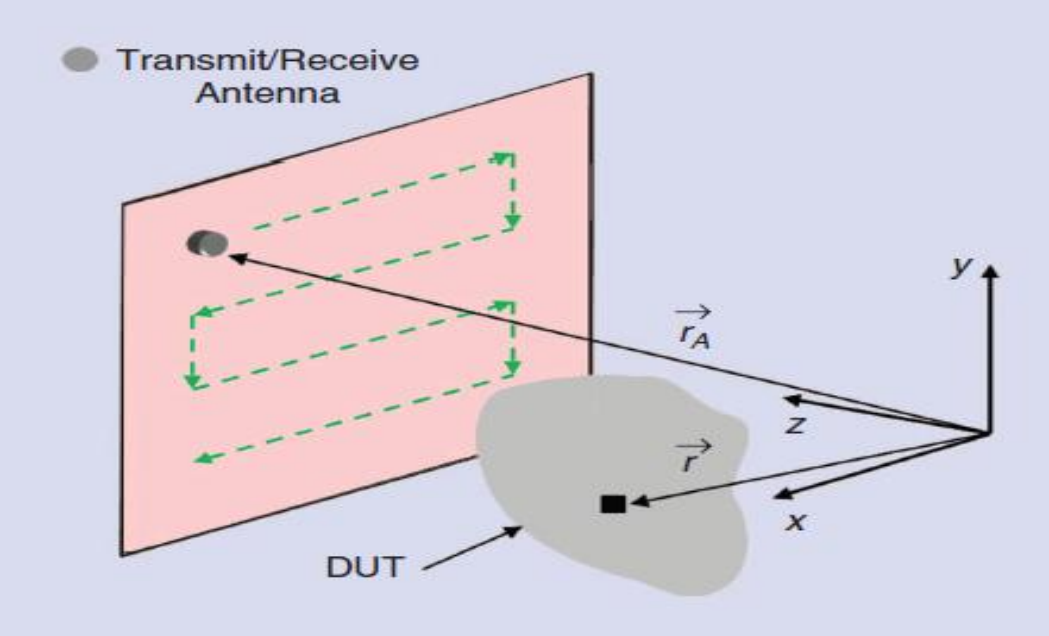

Figure 1: A schematic of a monostatic imaging set up [16]

However, for a detailed generalization imaging technique with several antenna positions (N_t , N_r), unique transmit and receive positions in the X and Y aperture, the phase history is as given is calculated

Hence, the response at the transceiver will essentially be the superposition of each point on the target, multiplied by the round-trip phase to that point where the target is assumed to be flat and parallel to the scan plane, that is, at constant z.

For a generalized imaging system with a multi-static set, the imaging algorithm reconstructs the reflectivity map $I\,(\,r\,)$ or image from the measured and recorded dataset, which shows the backpropagation algorithm as given in (5) [15].

$$I(r) = \sum_{N_f} \sum_{N_{Tx}} \sum_{N_{Rx}} S(\bar{r}_T, \bar{r}_R, f_n) e^{+j\frac{2\pi f_n}{c_0}(|r-r_{Tx}|+|r-r_{Rx}|)} \quad (5)$$

The value of the reconstructed reflectivity map of the target $I(r)$ is constructed at position r of the target.

In this study, the background subtraction method was employed to further enhance the algorithm's image reconstruction capabilities. Two distinct measurements were conducted to

assess the effectiveness of the BPA in conjunction with the frequency filtering technique. The first measurement was performed without the targets in the imaging setup, where the scattering parameter (amplitude and phase) of the reflected signal was recorded. A second measurement of the scattering parameter was then taken, this time with the targets included in the entire MWI setup. As noted by [18], a primary challenge with this measurement is the antenna-to-air mismatch. Since the antenna's reflection coefficient is consistent across the scanning area, the collected S_{11} data per frequency is averaged and then coherently subtracted from the averaged data [18].

$$S(x,y,f) = S_{11}(x,y,f) - \sum_y \sum_x \frac{S_{11}(x,y,f)}{N_y N_x} \quad (6)$$

where N_x and N_y are the number of sample points in the X and Y directions, respectively.

2.2 Holographic Image Reconstruction Algorithm

Holographic techniques generate three-dimensional images by connecting scattered fields with reference waveforms, as illustrated in Fig. 2. Holographic imaging techniques utilize three different wave types—light, acoustic, and electromagnetic—to collect amplitude and phase data of wavefronts scattered from a target object. A significant development in 3D holography utilizing electromagnetic waves was introduced in [19]. The authors' solution abolished the conventional far-field prerequisite, facilitating near-field operation. To diminish the spherical wavefronts produced in the near field, the method employed a Fourier transform step to split these wavefronts into planar wave components.

Previous methods dependent on Fresnel approximations encountered significant resolution constraints in near-field imaging. The holographic image reconstruction approach presented in [19] addressed these limitations by neglecting slowly fluctuating amplitude functions, which empirical evidence indicated had a negligible effect on image quality. Although amplitude impacts were minimal, phase information was essential, with meticulous phase management being a crucial factor in reconstruction accuracy.

The Fourier transform is fundamental to this approach and is computed efficiently by the Fast Fourier Transform (FFT). The resolution is solely constrained by diffraction when far-field approximations are disregarded, with these constraints influenced by factors such as frequency, aperture size, beamwidth of the source and receiver, and the distance to the target [19].

In imaging applications, two-dimensional reconstructions employ single-frequency data from two-dimensional antenna arrays, whereas three-dimensional reconstructions require multi-frequency data collected via two-dimensional planar arrays [20]. This adaptability underscores the algorithm's versatility in several imaging scenarios.

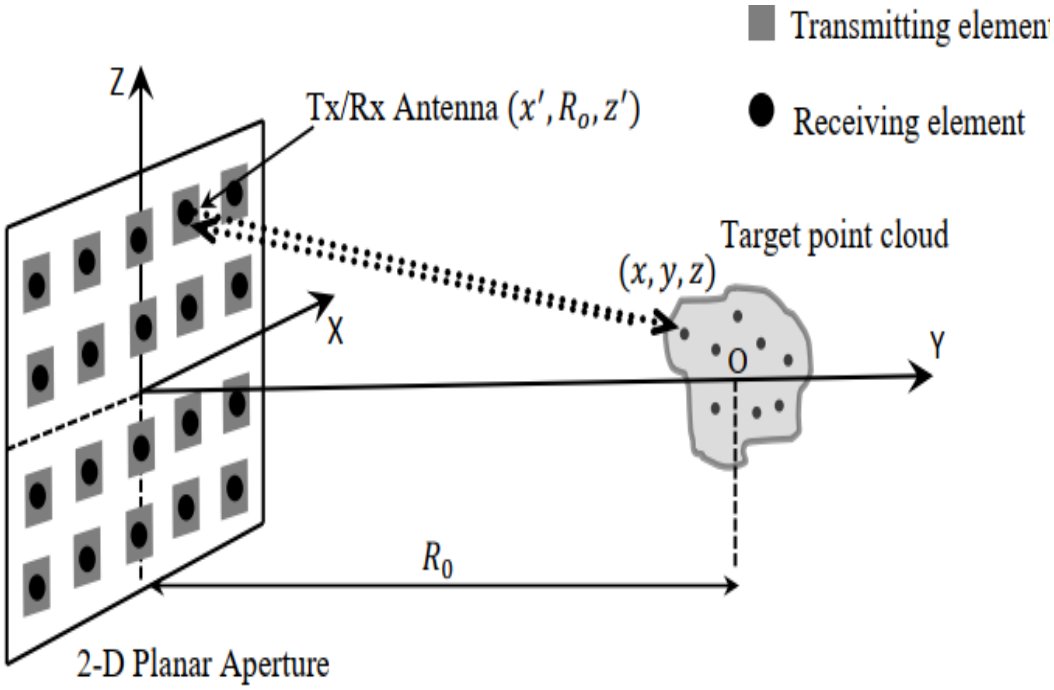

Figure 2: Imaging geometry of holographic image reconstruction algorithm [21]

Initially, the creation of a two-dimensional image is investigated. The antennas are situated at the coordinates (x', R_0, z') and the target points are presumed to be located at $(x,0,z)$. The target points are situated at the origin. The y-coordinate of the target space is regarded as constant for the reconstruction of a 2-D image utilizing single-frequency, k_1. In Equation (8), $D(x', z', k_1)$ denotes the signal scattered from a singular point target and received by an antenna situated at the coordinates (x', R_0, z'). The statement is formulated based on the Born assumption, which posits that interactions between point targets are disregarded; specifically, there is no interaction among the point targets. The solitary point is situated at $(x, 0, z)$, and the reflectivity of this singular point target is represented as $f(x, 0, z)$.

In its simplest form, $D(x', z', k_1)$ can also be expressed as shown in Equation (8) utilizing amplitudes and round-trip phase information of the signal. The distance between the antenna located at the coordinates (x', R_0, z') and the point scatterer situated at $(x, 0, z)$ is denoted as R [21].

$$R = \sqrt{(x - x')^2 + (R_0)^2 + (z - z^1)^2} \quad (7)$$

$$D(x', z', k_1) = f(x, 0, z).\frac{1}{4\pi R^2}.e^{-jk_1 2R} \quad (8)$$

The signal $S(x', R_0, z')$ received by the antenna at the location (x', R_0, z') corresponds to the scattered signals from all point targets within the scene. The wavenumber of the transmitted signal is denoted by k_1 and $f(x, 0, z)$ represents the target's reflectivity function. Consequently, $S(x', R_0, z')$ is the cumulative superposition of the signals scattered from all point targets, obtained by integrating $D(x', z', k_1)$ across the target space. During this process, the amplitude decay component from Equation (8) is excluded, as it has minimal impact on the final image, as described in Equation (9) [21].

$$S(x', z', k_1) = \iint f(x, 0, z) e^{-jk_1 2\sqrt{(x-x')^2+(R_0)^2+(z-z')^2}} dx dz \quad (9)$$

$k = \omega/c$, where ω is the temporal angular frequency and c is the speed of light. The exponential term given in Equation (9) can be decomposed into a superposition of plane wave components where k_x' and k_z' are the Fourier-transform variables corresponding to x' and z', respectively [10]. In Equation (10), k_y is y-component of the wavenumber vector of the plane waves [10].

$$e^{-jk_1 2\sqrt{(x-x')^2+(R_0)^2+(z-z^1)^2}} = \iint e^{jk_x'(x'-x)+jk_y(R_0)+jk_z'(z-z')}\, dk_{x'} dk_{z'} \quad (10)$$

Inserting Equation (10) into Equation (9) and assessing the expression yields Equation (11). The 2-D Fourier transform in the Equation serves as the foundation for the subsequent phase [10].

$$S(x', z', k_1) = \iint \left[\iint f(x, 0, z) e^{-j(k_x' x + k_x' z)} dx dz\right] \times \dots e^{j(k_x' x' + k_z' z' + k_x' R_0)} dk_{x'} dk_{z'} \quad \dots (11)$$

The expression within the square brackets represents the 2D Fourier Transform of $f(x, y_0, z)$. In Equation (9), if the reflectivity function $f(x, y_0, z)$ is treated as $f(x, z)$, applying the relations from (11) leads to Equation (12) [10].

$$S(x', z', k_1) = \iint F(k_x, k_z).\, e^{jk_y R_o}.\, e^{j\left(k_x' x' + k_z' z'\right)} dk_{x'} dk_{z'} \tag{12}$$

According to the Fourier Transform Theorem, $s(x', z')$ is the inverse Fourier Transform of the $F(k_x, k_z).\, e^{jk_y R_o}$ term as given in Equation (13) [10].

$$S(x', z', k_1) = FT_{2D}^{-1}\left[F(k_x, k_z) e^{jk_y R_0}\right] \tag{13}$$

The objective is to determine $f(x, z)$, the desired reflectivity function. This is achieved by deriving the reflectivity function in Equation (14) through the application of Fourier Transform relations [21].

$$F(k_x, k_z).\, e^{jk_y y_o} = FT_{2D}[S(x', z', k_1)] \tag{14}$$

$$F(k_x, k_z) = FT_{2D}[S(x', z', k_1)].\, e^{-jk_y R_o} \tag{15}$$

$$F(x, z) = FT_{2D}^{-1}\left[FT_{2D}[S(x', z', k_1)] e^{-jk_y R_o}\right] \tag{16}$$

The wave number component k_y is derived from the dispersion relation, as presented in Equation 18 [21].

$$k_x^2 + k_y^2 + k_z^2 = (2k_1)^2 \tag{17}$$

$$k_y = \sqrt{4{k_1}^2 - k_x^2 - k_z^2} \tag{18}$$

It is important to note that k_y in Equation (18) must remain positive. Field modes satisfying the inequality $\left(4{k_1}^2 > k_x^2 + k_z^2\right)$ represent the propagating modes, while those that

do not are classified as evanescent modes. Additionally, the reconstruction algorithm is outlined in Equation (19) [21].

$$F(x,z) = FT_{2D}^{-1}\left[FT_{2D}[S(x',z',k_1)]e^{-j\sqrt{4{k_1}^2-k_x^2-k_z^2}.(R_o)}\right] \quad (19)$$

The steps used for implementing the Holographic /Stolt migration technique are outlined as follows:

Step 1: Obtain the frequency domain data set, $S(f,x,y)$

Step 2: Take the FFT along the x-axis

Step 3: Perform Mapping to the z-axis

Step 4: Perform Stolt Interpolation technique using the wave dispersion model in k_z domain

Step 5: Perform 2-D inverse FFT of the data obtained to get the 2-D reflectivity image

2.2.1 Spatial and frequency sampling

Data acquisition and picture reconstruction necessitate that the incoming data is sampled discretely. Successful sampling necessitates adherence to the Nyquist sampling criterion. The factors influencing the requisite sampling across the aperture include the wavelength, aperture dimensions, target size, and distance to the target. The Nyquist requirement for spatial sampling is fulfilled when the phase shift between consecutive sample points is less than π radians. Consequently, the antenna spacing criterion is articulated in Equation (20), indicating that practical imaging systems frequently utilise sample intervals about equal to $\lambda/2$ [23].

$$\Delta x < \frac{\lambda_{min}}{2} \quad (20)$$

The required frequency sampling is determined in a similar way as given in Equation (21) where ΔR is the length of target space in the range direction [23].

$$\Delta f < \frac{c}{2.\Delta R} \quad (21)$$

On the other hand, the number of frequency samples for a bandwidth B must be as in Equation (22) where the number of frequency samples is given as $N_f = B/\Delta f$ [23].

$$N_f > \frac{2.B.\Delta R}{c} \quad (22)$$

2.2.2 Range and cross-range resolutions

This section discusses an image-reconstruction technique that utilizes 2-D FFT to create the image in the spatial frequency domain. The image resolution can be readily ascertained by analyzing the width of the coverage in the spatial frequency domain. In order to achieve a successful image reconstruction, the discretization of the frequency band and the sampling domain requires that the Nyquist sampling criterion be satisfied [24].

For a spatial sample interval of Δx, the sampling criterion is expressed as [24];

$$\Delta x < \frac{\lambda R}{D} \quad (23)$$

where $\lambda = 2\pi/k$ is the wavelength, $R =$ the target distance from the antenna, $D =$Scanning length of the aperture

The required frequency sampling is arrived at by the expression in (24) [24].

$$\Delta f \leq \frac{c}{4R_{max}} \quad (24)$$

R_{max} is the maximum target range, Δf is the required frequency sampling interval

Invariably, the number of frequency samples for a bandwidth, B must be equivalent to the expression in (25) [24].

$$N_f > \frac{2R_{max}}{(c/2B)} \quad (25)$$

Equation (25) highlights that two frequency samples are needed for each range-resolution cell, where the range resolution is given as $c/2B$.

3. MATERIALS AND METHODS

3.1 Experimental Setup

A picture of the experimental setups showing the different obstructions concealing the targets is presented in Fig. 3. A monostatic image setup consisting of an ultrawideband horn antenna with a resonance frequency between $15\,GHz$ and $22\,GHz$ was used as both the transmitting and receiving antenna. The measurement setup also includes a Vector Network Analyzer which the horn antenna is connected. The VNA generates a stepped frequency, and it is configured to obtain measurements within $15\,GHz$ and $22\,GHz$ frequency bands. Additionally, the setup features an automated 2-D scanner that enables the X and Y coordinates of the scanning range for the microwave imaging monostatic system. The targets, as shown in Fig. 4, consist of copper materials sculptured from capital letters of the alphabet "NCAT." The targets are of varying heights and sizes; this enables us to determine how small the targets can reach without being detected and producing a distinguished spatial resolution. The target used for this work consists of multiple copper letters spelling 'NCAT' fabricated in varying sizes (as shown in Fig. 3). The first row of target alphabets is 12 cm in height and width, the second row of targets is 7 cm in height and width while the first two letters of the third row is 3.5 cm in height and width. Due to Copper's high conductivity, the letters act as strong reflectors to the incident microwave signals. The presence of multiple letters, each with unique dimensions and orientations, introduces complex scattering effects, resulting in multiple reflections observed in the cross-range profiles.

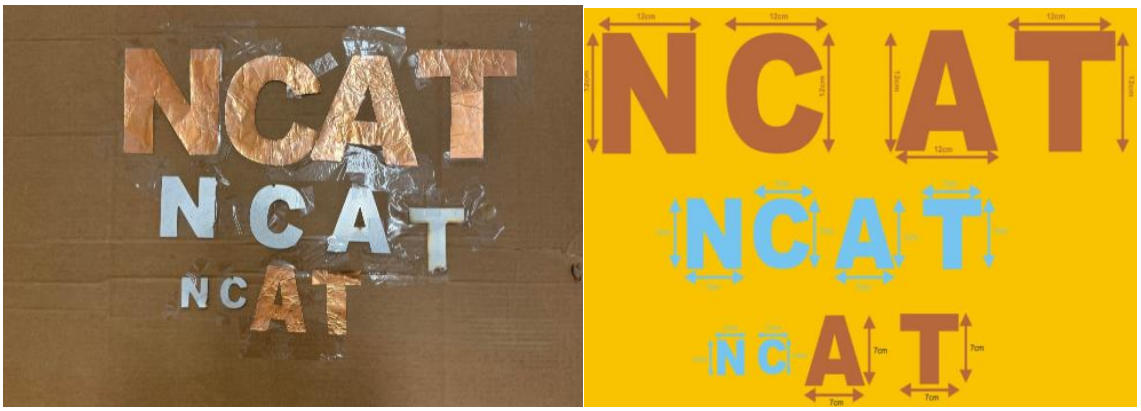

(a) (b)

Figure 3: Alphabetical letter target (a) Physical depiction (b) Dimensions

The targets are attached to a hard paper board, which serves as the imaging plane for the monostatic MWI setup. The range resolution of the target to the antenna is $0.94\ m$. To perform the monostatic imaging process, the horn antenna is moved along the X and Y coordinates of the scanner with a dimension of $50\ cm\ \times\ 50\ cm$. The step size used along each of the coordinates is $1\ cm$. This makes the total imaging aperture discretized N points (N_x and N_y) to be 2500 points. The S_{11} scattering parameters are obtained at each point for each frequency.

Figure 4: Wet cloth concealing the targets

The first experimental setup consists of a wet cloth covering the target as the barrier, as shown in Fig. 5. The water-soaked wet cloth helped to determine how lossy the reflected microwave signals are and if it can detect the targets covered by the wet cloth. The second experimental (Fig. 6) setup replaced the wet cloth with a flexible granite wall, which has a thickness of $3\ mm$ to conceal all the targets. All the experimental parameters remained constant.

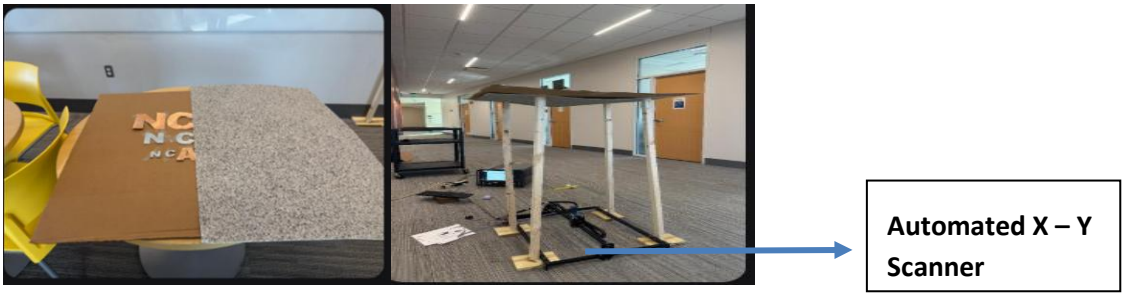

Figure 6: Targets covered with granite wall

For the third experiment setup, a rectangular wood was used to cover the targets, as illustrated in Fig. 7. The thickness of the wood is one and a half inches, and all the parameters of the experiment remained constant.

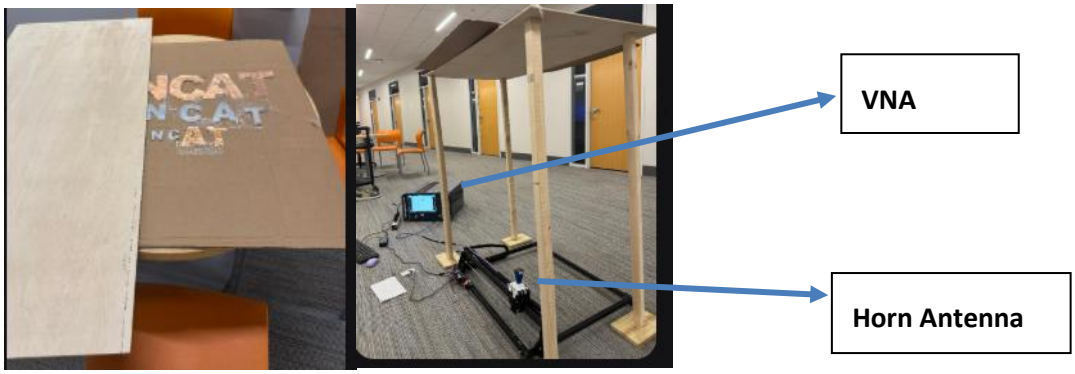

Figure 7: Targets covered with wood

For the fourth experiment setup, a thick granite tile with a thickness of 12.7 mm was used to cover the targets, as illustrated in Fig. 8. The experiment was performed with all other system parameters constant.

Figure 8: Targets covered with Tile

For all four monostatic experimental setups, in each antenna position, the measured scattering parameters are stored in the VNA memory as an *s1p* file and then transferred to a PC for processing in MATLAB using the BPA and holographic algorithm to reproduce the images of the concealed targets. The depth of the spatial resolution of the images reconstructed from each algorithm was compared, and the computational time of the algorithms was also determined to assess their computational efficiency. Table 1 also highlights the various

scientific properties of the materials used to conceal the targets. The permittivity and loss tangent values are shown as this allows us to understand the effect of the materials on the reflection, absorption and attenuation of the reflected microwave signals.

Table 1: The Characteristics of the Materials Concealing the Targets

Material	Thickness (mm)	Permittivity, ε	Loss Tangent, tan δ
Wet Cloth	0.3	10	0.1 - 0.5
Flexible Granite Wall	3	4	0.02 - 0.05
Dry Wood	12.7	3	0.01 - 0.05
Granite Tile	12.7	7	0.01 – 0.05

Source: [25]

3.2 Calibration Procedure

In this study, the one-port calibration method—short, open, load (SOL) was applied to measure errors and calibrate the VNA measurement system. This step is important because it helps to correct the phase and amplitude errors resulting from measurement setup. Initially, the VNA system assumed no measurement error, and then measurements were taken using the SOL calibration kit. The reference plane of the VNA was set to the end of the VNA cables by performing the SOL calibration with a mechanical calibration kit.

4. RESULTS AND DISCUSSION

4.1 BPA and Holographic with Target Concealed with Wet Cloth

The BPA and Holographic algorithms have been used to reconstruct the scenario from scattering parameters obtained after the microwave signals were reflected from the targets. The images of the target reproduced by the BPA are shown in Fig. 9 (a). From the image, it can be seen that the spatial resolution of the images of the target is high. This is so because the target details and edges can be perfectly defined. Also, the exact positions of the targets align perfectly with the positions of the targets. The image reconstructed also showed how small the targets can be in order to achieve a perfect spatial resolution, as the smaller letters on the last row were not highly defined. A drawback of the BPA is the simulation time is quite high when compared

to that of the holographic algorithm. Hence, it has a very low computational efficiency, and it is not suitable for large data set imaging. On the other hand, the image reproduced when we applied the holographic algorithm (Fig. 9 (b)) has a very low spatial resolution. The images cannot be clearly defined even though the overall shape of the targets is quite conspicuous. The images are blurry and contain artifacts.

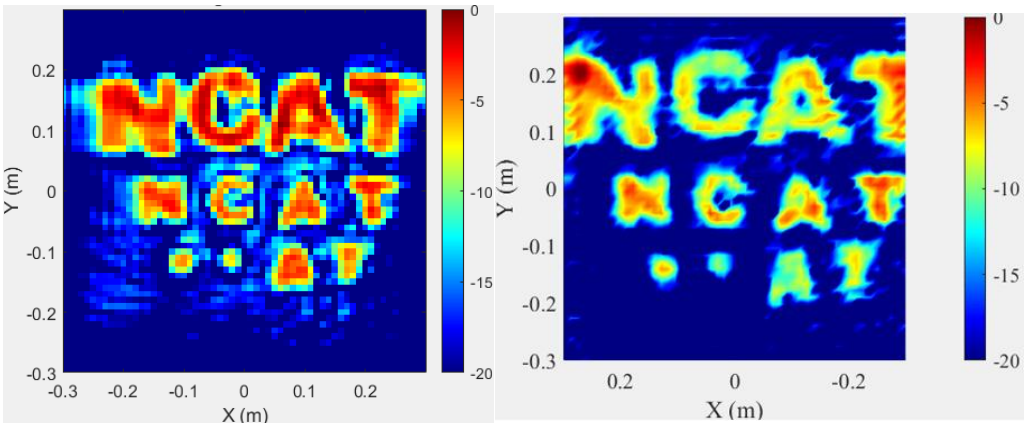

(a) (b)

Figure 9: Reconstructed images of wet concealed targets (a) 2D – BPA (b) 2D –Holographic

4.2 BPA and Holographic Algorithm with Targets Concealed with Granite Wall

A 3-mm-thick flexible granite wall obscured the targets. As illustrated in Fig. 10 (a), the BPA effectively reconstructed high-resolution images of the targets despite the presence of the obscuring obstacle. This demonstrates the capability of microwave signals to penetrate certain materials and detect concealed objects. The BPA achieved sharp spatial resolution, with target edges and fine details clearly defined, owing to its coherent summation of reflected signals to highlight regions of high reflectivity. In contrast, Fig. 10 (b) reveals that the holographic algorithm produced images with significantly lower resolution, characterized by blurring and artifacts. While the holographic method underperformed in image clarity, it offers advantages in computational efficiency, processing speed, and reduced resource requirements. Thus, BPA is preferable for applications demanding precision, whereas the holographic algorithm may suffice in scenarios prioritizing rapid, low-cost imaging.

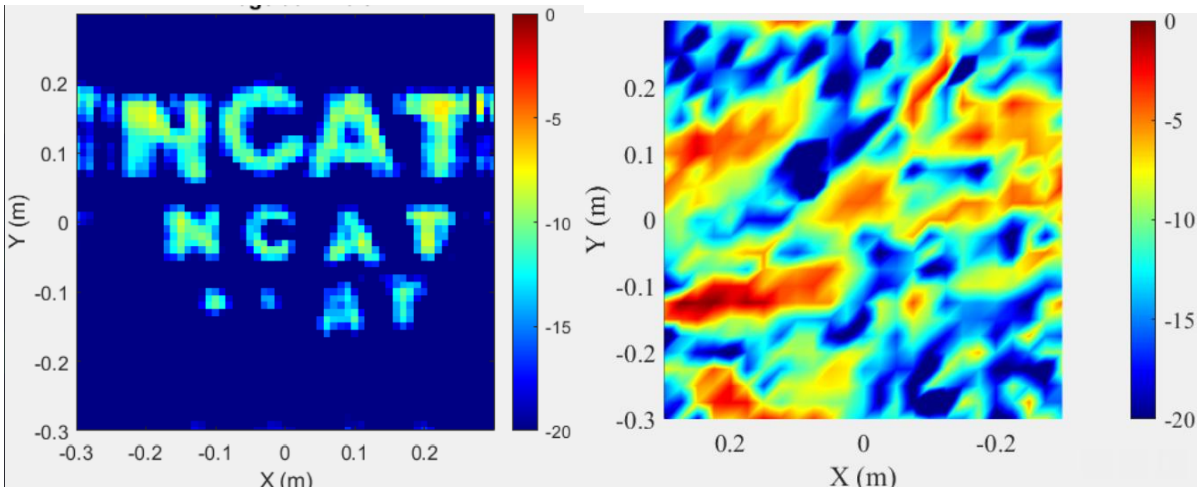

(a) (b)

Figure 10: Reconstructed images of granite-wall concealed targets (a) 2D – BPA (b) 2D – Holographic

4.3 BPA and Holographic Algorithm with Targets Concealed with Wood

The targets were concealed behind a 12.7-mm-thick wooden barrier. As shown in Fig. 11 (a), the BPA successfully reconstructed images of the targets on the second row and first row. However, the spatial resolution was notably lower compared to results from wet cloth and granite wall barriers. This also can be attributed to the large amount of attenuation suffered by the reflected signals from the targets. The reconstructed images exhibited blurring, with target edges and poorly defined details. In contrast, the holographic algorithm (Fig. 11 (b)) produced even less clarity than the BPA, with significant artifacts further degrading resolution. These distortions rendered the holographic images indistinct, underscoring the BPA's superior ability to resolve obscured targets despite its reduced performance relative to other obstacle materials. It can be observed that the first row of targets was ghostly reproduced; this is probably due to the wearing out of the adhesive holding down the antenna as the experiment progresses thereby not giving accurate reflected signals from the targets of the first row.

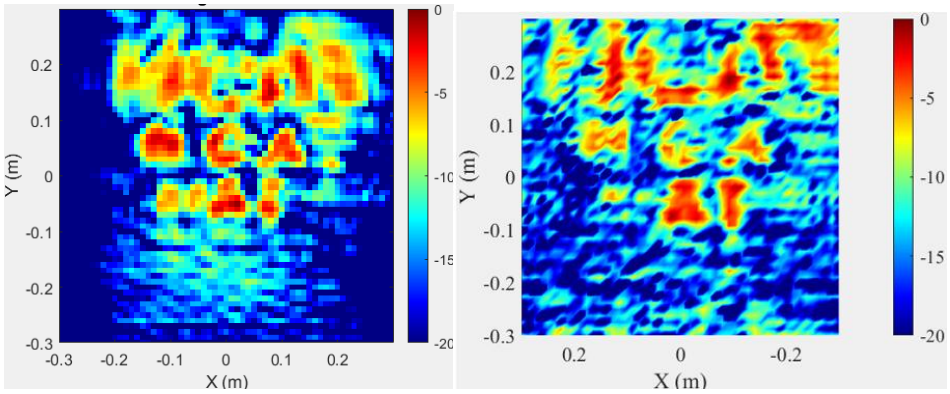

(a) (b)

Figure 11: Reconstructed images of wood concealed targets (a) 2D – BPA (b) 2D – Holographic

4.4 BPA and Holographic Algorithm with Targets Concealed with Tile

The targets were concealed behind a 12.7-mm-thick tile barrier. As shown in Fig. 12 (a), the BPA successfully reconstructed images of the first-row targets (the largest targets) this can be attributed to the less attenuation suffered by reflected signals. However, reflected signals from the other smaller targets were seen to be attenuated because the images of these sets of targets were not reconstructed. But rather shows as clutter and artifacts. However, the spatial resolution was notably lower compared to results from wet cloth and granite wall barriers. The reconstructed images exhibited blurring, with target edges and details poorly defined. In contrast, the holographic algorithm (Fig. 12 (b)) produced even less clarity than the BPA, with significant artifacts further degrading resolution. These distortions rendered the holographic images indistinct, underscoring the BPA's superior ability to resolve obscured targets despite its reduced performance relative to other obstacle materials.

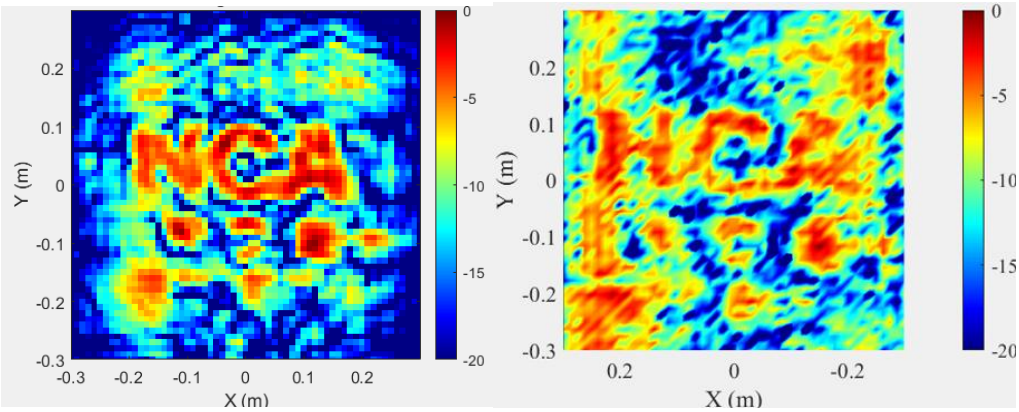

(a) (b)

Figure 12: Reconstructed images of tile concealed targets (a) 2D – BPA (b) 2D –Holographic

The time taken for the BPA to run for all four experimental setups is 7065 seconds, and the time taken by the holographic algorithm is 115 seconds on average. This accentuates that the computational efficiency of the holographic algorithm is better than the BPA.

The first step is to determine the frequency step size, Δf. The frequency of operation of my horn antenna is $15\ GHz$ to $22GHz$. The frequency step size, Δf is evaluated as follows:

$$\Delta f = \frac{22GHz - 15GHz}{2001 - 1} = 3.5\ MHz$$

The maximum range that can be constructed depends on the total bandwidth and frequency step size evaluated as follows:

$$R_{max} = \frac{3 \times 10^8}{2 \times (3.5 \times 10^6) \times 2001} = 21.4m$$

In order to ensure the Nyquist criterion is satisfied along the spatial sampling interval aloing the scanning aperture. The wavelength at the highest operating frequency of $22GHz$ is $0.0136m$.

$$\Delta x \leq \frac{0.0136 \times 0.94}{0.5} = 0.0256\ m\ (2.56\ cm)$$

Since the chosen scanning step size is $1cm$, which is smaller than the required $2.56cm$, the Nyquist criterion is achieved. This ensures the accuracy of image reconstruction and prevents spatial aliasing.

5. CONCLUSION

In this work, a portable, low-cost monostatic microwave imaging system and algorithm were presented. It was shown that the BPA demonstrated superior spatial and cross-range resolution, effectively reconstructing concealed targets' fine structural details compared to the holographic algorithm, which exhibited limited resolution under identical experimental conditions. While BPA achieved enhanced image fidelity through point-wise phase compensation and coherent summation across spatial and frequency domains, it incurred

significantly higher computational complexity and processing time. In contrast, holographic algorithms prioritized computational efficiency through spectral-domain processing and fast convolution, enabling rapid large-scale imaging at the expense of resolution. Also, the holographic algorithm tends to reproduce the images of the targets with a higher number of antenna scan positions, which is one of the limitations encountered in this research. The antenna scanned positions were limited to 50×50 with a total point of 2500. The cost of system complexities associated with BPA is higher and hence results in longer simulation time. Consequently, algorithm selection was application-specific: holographic methods were suited to real-time, low-latency applications like ultrasound imaging and wide-area surveillance, whereas BPA excelled in high-resolution detection tasks such as security screening, non-destructive evaluation, and biomedical diagnostics. Although holographic-based approaches offered scalability and speed, they underperformed relative to BPA in resolving fine spatial features, particularly in complex or high-attenuation environments.

ACKNOWLEDGEMENT

The author would like to express appreciation to the Joint School of Nanoscience and Nanoengineering, North Carolina A & T State University for their contributions on this project.

REFERENCE

[1] S. Ahmed, J. Thompson, and R. Smith, Monostatic vs. multistatic microwave imaging: A cost-resolution trade-off analysis, *J. Nondestruct. Eval.*, vol. 39, no. 3, pp. 1–14, 2020.

[2] X. Chen, Y. Li, and Z. Wang, Microwave imaging through dielectric barriers: Penetration capabilities and resolution limits, *IEEE Trans. Microw. Theory Tech.*, vol. 69, no. 4, pp. 2012–2025, 2021.

[3] A. C. Gurbuz, J. H. McClellan, and W. R. Scott, High-resolution backpropagation for concealed object detection, *IEEE Geosci. Remote Sens. Lett.*, vol. 16, no. 7, pp. 1099–1103, 2019.

[4] S. Gupta, C. Li, and R. Narayanan, Compressive holographic microwave imaging for rapid data acquisition, *IEEE Trans. Comput. Imaging*, vol. 6, pp. 1343–1355, 2020.

[5] T. Hassan, M. Al-Mistarihi, and M. Al-Sa'd, Algorithmic cost-benefit analysis in security and medical microwave imaging, *IEEE J. Biomed. Health Inform.*, vol. 27, no. 2, pp. 789–800, 2023.

[6] D. Kim, S. Park, and H. Lee, Holographic microwave imaging with phase retrieval for rapid object detection, *Sensors*, vol. 21, no. 9, p. 3056, 2021.

[7] L. Martinez and S. Khan, Adaptive holographic imaging for dynamic material environments, *IEEE Trans. Antennas Propag.*, vol. 71, no. 5, pp. 4120–4131, 2023.

[8] D. O'Connor, J. Walsh, and D. Byrne, Frequency-hopping techniques for multi-layered barrier imaging, *Microw. Opt. Technol. Lett.*, vol. 64, no. 8, pp. 1432–1440, 2022.

[9] R. Patel, Y. Zhang, and M. Liu, Machine learning-enhanced backpropagation for microwave imaging, *IEEE Trans. Artif. Intell.*, vol. 2, no. 4, pp. 321–333, 2021.

[10] R. Singh, A. Kumar, and N. Gupta, Electromagnetic properties of common barrier materials: Implications for microwave imaging, *Mater. Today: Proc.*, vol. 33, pp. 2105–2110, 2020.

[11] Y. Wang, Q. Zhang, and F. Liu, Hybrid backpropagation-holography for depth-resolved microwave imaging, *Opt. Express*, vol. 30, no. 12, pp. 21589–21604, 2022.

[12] L. Zhang and H. Zhao, GPU-accelerated backpropagation for real-time microwave imaging, *IEEE Access*, vol. 10, pp. 34567–34578, 2022.

[13] W. C. Chew, *Waves and Fields in Inhomogeneous Media*. New York, NY, USA: IEEE Press, 1995.

[14] T. M. Grzegorczyk, P. M. Meaney, and K. D. Paulsen, Fast 3-D tomographic microwave imaging for breast cancer detection, *IEEE Trans. Med. Imaging*, vol. 31, no. 8, pp. 1584–1592, 2012.

[15] T. Spreng et al., UWB near-field MIMO radar: Calibration, measurements and image reconstruction, *Proc. 10th Eur. Radar Conf.*, 2013, pp. 33–36.

[16] S. S. Ahmed et al., Advanced microwave imaging, *Proc. IEEE Microw. Mag.*, vol. 13, no. 6, pp. 8–10, 2012, doi: 10.1109/MMM.2012.2205772.

[17] D. M. Sheen and T. E. Hall, Reconstruction techniques for sparse multistatic linear array microwave imaging, *Proc. SPIE*, vol. 9078, p. 90780I, 2014, doi: 10.1117/12.2053814.

[18] M. Fallahpour et al., Piecewise and Wiener filter-based SAR techniques for monostatic microwave imaging of layered structures, *IEEE Trans. Antennas Propag.*, vol. 62, no. 1, pp. 282–294, 2014, doi: 10.1109/TAP.2013.2287024.

[19] D. M. Sheen, D. L. McMakin, and T. E. Hall, Three-dimensional millimeter-wave imaging for concealed weapon detection, *IEEE Trans. Microw. Theory Tech.*, vol. 49, no. 9, pp. 1581–1592, 2001, doi: 10.1109/22.942570.

[20] A. V. Muppala et al., Fast-Fourier Time-Domain SAR Reconstruction for Millimeter-Wave FMCW 3-D Imaging, *IEEE Trans. Microw. Theory Tech.*, pp. 1–11, 2024, doi: 10.1109/TMTT.2024.3406938.

[21] A. B. Duysak, A. T. Öztürk, and A. Genç, Conical differential range-based back-projection algorithm for three-dimensional millimeter-wave imaging, *Trait. Signal*, vol. 39, no. 6, pp. 2031–2041, 2022, doi: 10.18280/ts.390610.

[22] D. M. Sheen, D. L. McMakin, and T. E. Hall, Three-dimensional millimeter-wave imaging for concealed weapon detection, *Proc. SPIE*, vol. 49, no. 9, pp. 106–117, 2001.

[23] D. M. Pozar, *Microwave Engineering*, 4th ed. Hoboken, NJ: Wiley, 2011.

Citation: Babatunde Olatujoye, Binbin Yang. (2025). Resolution, Computational Efficiency, and Cost Analysis of Backpropagation and Holographic Algorithms for Concealed Object Detection Through Various Materials Using Monostatic Microwave Imaging. International Journal of Electronics and Communication Engineering (IJECEG), 2(1), 24-47.

Abstract Link: https://iaeme.com/Home/article_id/IJECEG_02_01_003

Article Link:
https://iaeme.com/MasterAdmin/Journal_uploads/IJECEG/VOLUME_2_ISSUE_1/IJECEG_02_01_003.pdf

✉ **editor@iaeme.com**